Biophysical Journal
Article

Biophysical Society

Deformability and collision-induced reorientation enhance cell topotaxis in dense microenvironments

Leonie van Steijn,[1,*] Joeri A. J. Wondergem,[2] Koen Schakenraad,[1,2] Doris Heinrich,[3,4,5] and Roeland M. H. Merks[1,6]

[1]Mathematical Institute, Leiden University, Leiden, the Netherlands; [2]Leiden Institute of Physics, Leiden University, Leiden, the Netherlands; [3]Fraunhofer Institute for Silicate Research ISC, Würzburg, Germany; [4]Institute for Bioprocessing and Analytical Measurement Techniques, Heilbad Heiligenstadt, Germany; [5]Faculty for Mathematics and Natural Sciences, Technische Universität Ilmenau, Ilmenau, Germany; and [6]Institute of Biology, Leiden University, Leiden, the Netherlands

ABSTRACT In vivo, cells navigate through complex environments filled with obstacles such as other cells and the extracellular matrix. Recently, the term "topotaxis" has been introduced for navigation along topographic cues such as obstacle density gradients. Experimental and mathematical efforts have analyzed topotaxis of single cells in pillared grids with pillar density gradients. A previous model based on active Brownian particles (ABPs) has shown that ABPs perform topotaxis, i.e., drift toward lower pillar densities, due to decreased effective persistence lengths at high pillar densities. The ABP model predicted topotactic drifts of up to 1% of the instantaneous speed, whereas drifts of up to 5% have been observed experimentally. We hypothesized that the discrepancy between the ABP and the experimental observations could be in 1) cell deformability and 2) more complex cell-pillar interactions. Here, we introduce a more detailed model of topotaxis based on the cellular Potts model (CPM). To model persistent cells we use the Act model, which mimics actin-polymerization-driven motility, and a hybrid CPM-ABP model. Model parameters were fitted to simulate the experimentally found motion of *Dictyostelium discoideum* on a flat surface. For starved *D. discoideum*, the topotactic drifts predicted by both CPM variants are closer to the experimental results than the previous ABP model due to a larger decrease in persistence length. Furthermore, the Act model outperformed the hybrid model in terms of topotactic efficiency, as it shows a larger reduction in effective persistence time in dense pillar grids. Also pillar adhesion can slow down cells and decrease topotaxis. For slow and less-persistent vegetative *D. discoideum* cells, both CPMs predicted a similar small topotactic drift. We conclude that deformable cell volume results in higher topotactic drift compared with ABPs, and that feedback of cell-pillar collisions on cell persistence increases drift only in highly persistent cells.

SIGNIFICANCE Knowing how the environment influences cell motility is useful in developing methods to interfere during disease or in tissue engineering. One factor is the presence of obstacles: in a process called topotaxis single cells move from a high to a low density of obstacles. Here, we show that a number of cellular properties, namely deformable volume, contact inhibition of locomotion, and adhesiveness to obstacles, influence the efficiency of topotaxis. Understanding the differences in these properties between cell types could point to cell sorting mechanisms for tissue engineering, or shed light on the migratory behavior of immune and cancer cells.

INTRODUCTION

Motile cells moving through tissue encounter many obstacles, such as other cells and the extracellular matrix. How cells react to the density of obstacles is important for many biological processes, such as cancer cells invading from a dense tumor into looser packed tissues (1,2), immune cells moving through tissues with different porosity (3,4), or pathogens such as *Plasmodium* that migrate through different tissues throughout their life cycle (5,6). Recently, various in vitro assays provided experimental evidence that cells use the topography of their environment to actively orient themselves (5,7–11). Although topographically induced cell migration has predominantly been shown for in vitro environments, it is likely to also play a role in vivo, as the typical cellular environment contains a rich variety of

Submitted October 7, 2022, and accepted for publication June 2, 2023.

*Correspondence: l.vansteijn@uu.nl

Leonie van Steijn's present address is Theoretical Biology & Bioinformatics, Universiteit Utrecht, Utrecht, the Netherlands.

Editor: Pablo Iglesias.

https://doi.org/10.1016/j.bpj.2023.06.001

© 2023 Biophysical Society.

physical structures ranging from the nanometer to millimeter scale.

Topotaxis is an excellent umbrella term to describe all such forms of biased cell migration caused by asymmetries in the topography of the cellular environment. Recently, the term was reintroduced by Park et al. to describe topographic cell guidance by subcellular pillar geometries (7). Such assays, with topotactic cues at the subcellular scale, result in uninterrupted physical feedback between the cell body and the topographic asymmetry, which was shown to result in biased motion for various configurations (7–10). However, for highly motile persistent random cell motion, topotaxis can also be generated by topotactic cues, which span distances much larger than the typical cell body, as shown by Wondergem et al. (12). In these experiments, *Dictyostelium discoideum*, a model organism used to study persistent random cell motion (13), was shown to drift into areas of lower obstacle density and increased spacing over long distances. The spacing between subsequent rows of obstacles (pillars of cell size) was only increased after multiple cell lengths, introducing changes in topography at distances beyond the cell size. Hence, in these experiments, the cell body was not in continuous contact with the topographic asymmetry, in contrast to the nanoscale and microscale structures described in (7,10). Yet, the asymmetric pillar grid provided a sufficiently strong topographic cue to cause a net drift of approximately 5% of cell speed over large distances, even when exposed to competing chemotactic cues.

For such long-distance topotaxis to occur, Schakenraad et al. (14) hypothesized that the drift could be the result of local differences in the effective persistence of cell motion, which is continuously modified by various cell-obstacle interactions. Using active Brownian particles (ABPs) as a model system for cell motion, they showed that this is indeed the case. Particle trajectory simulations in anisotropic pillar fields resulted in local differences in persistence and to a net topotactic drift (14). Such positionally dependent kinesis was first suggested as a contributing cause for bacterial chemotaxis (15) where cells tumble more frequently in lower chemoattractant concentrations, and for observed durotaxis on stiffness gradients (16) where cells on softer substrates change direction more slowly than on stiffer substrates. However, the ABP model underestimates the topotactic effect measured for live cells, finding a 1% drift compared with particle speed, which is lower than the 5% observed for *Dictyostelium*. The ABP model simulated the cell as an undeformable disk moving at a constant speed and mediated particle-pillar interactions through a simple hard-wall force. Both choices allow for a very intuitive study into the role of persistence in topotactic drift, but leave out any intricacies posed by the dynamically changing cell body while navigating complex environments.

Here, we explore more refined models of cell migration, and, more specifically, investigate if either the deformable cell body or more complicated cell-pillar interactions play a pivotal role in long-distance topotaxis. The cell body likely influences migration through the obstacle fields, as the cell needs to undergo various morphological changes to squeeze through the pores between pillars. Moreover, when moving through the pillar field, cells are not guided around pillars at constant velocity by a hard-wall force as ABPs, but, for example, reorient more similar to contact inhibition of locomotion (CIL). To investigate different types of cell-pillar interactions, and gauge the influence of the cell body, we tested two different methods of persistent random motion within the framework of the cellular Potts model (CPM). The first method is based on the Act model, which models cytoskeletal rearrangements (17). This actin-extended CPM allows for emergent, active reorientation, as the cell cannot extend into a pillar and will be nudged to repolarize after the interaction, similar to CIL. The second method is a hybrid ABP-CPM model, which excludes any possibility of CIL, as the direction of preferred motion of the simulated cell changes solely based on an inherent characteristic persistence time, but irrespective of obstacle interactions, similar to the ABP model. Although pillars are unable to alter the inherent persistence in the ABP-CPM, the simulation does retain any influence of the deformable cell body on cell migration through the pillar grid. The parameters of the CPM, and both associated methods of driving persistent random motion, were empirically calibrated by measuring *D. discoideum* migration on flat surfaces.

The CPM simulations of the two methods of persistence resulted in a different topotactic response. The ABP-CPM simulations resulted in more topotactic drift than ABPs for the same motion parameters, clearly demonstrating the influence of a deformable cell body on the efficiency of topotactic response. The Act-CPM simulations exhibited the most pronounced topotactic drift, which we show can be attributed to changes in both speed and persistence by simulating cell motion in pillar grids of constant spacing. To compare the simulations with experimental data, we measured the topotactic drift for starved *D. discoideum* migrating on the pillar field introduced by Schakenraad et al. (14), which allows for a continuously changing linear gradient, contrary to earlier experimental work. Measuring cell migration on the same lattices used for modeling topotaxis ensured a more optimal comparison between experimental and simulated data. The ABP-CPM most closely matches the experimental topotactic drift, whereas the Act-CPM slightly overpredicts topotaxis. However, when normalizing for cell speed, the measured topotactic drift of *D. discoideum* sits between the ABP-CPM and Act-CPM simulated drifts. Finally, we tested the effect of changing the adhesion energy between cells and pillars. Changing this adhesion energy has a direct influence on

the cell speed next to pillars, and thereby topotactic drift, and equates to varying the surface material of the pillars in in vitro assays.

MATERIALS AND METHODS

For this study, we have used an experimental setup with live cells and three computational models. Experimental data from cells on a flat surface were used to set the model parameters and calibrate the simulations. Topotaxis caused by gradients of anisotropically placed cell-sized obstacles (pillars) was investigated in experimental assays, as well as in computational models.

Live-cell experiments

Cell culture and experiment preparation

For all migration experiments, axenic *D. discoideum* (Ax2) with a cytoplasmic green fluorescent protein (GFP) insertion was used (strain HG1694, obtained from Dr. G. Gerisch, MPI for Biochemistry, Martinsried, Germany). Cells were grown at 20°C in HL5 medium, supplemented with 20μg mL^{-1} gentamicin (Gentamycin solution, Merck, the Netherlands) as a selection antibiotic. The cells were cultured in 100 mm petri dishes (100 mm TC-treated culture dish, Corning, Corning, New York) and confluency was kept below 70% during culturing. For visualizing actin polymerization, a LimE-GFP in lim0 cell line was used (18). These cells were cultured similarly, but with two selection antibiotics instead, 10 μg mL^{-1} gentamycin and 10 μg mL^{-1} blasticidin, necessary to maintain the double mutation (LimE-GFP and Lim0).

In preparation for imaging experiments, cells were harvested by Pipette-induced flow and collected in a conical tube. To remove the culture medium, the cells were centrifuged at 1500 rpm for 3 min. In the case of vegetative experiments, resulting cell pellets were thrice washed using nonfluorescent buffer (3.6 mM KH_2 PO_4, 2.9 mM Na_2 HPO_4 [pH 6.7]) and, after resuspension, transferred onto (un)structured polydimethylsiloxane (PDMS) surfaces placed inside an imaging chamber (see obstacle and flat PDMS surfaces). In the case of starved experiments, a pulsation procedure was started before imaging instead. Cell pellets were thrice washed with 17 mM K-Na-phosphate-buffered saline (PBS) (pH 6.0) and placed on a shaker for 1 h. Then, to induce cAR1 expression, cells were pulsed with 150 nM cyclic adenosine-monophosphate (cAMP) (Merck, Amsterdam, the Netherlands) applied in 6 min intervals over 4 h while shaking. After pulsation, any residual cAMP was removed by centrifugation and resuspension. Cells were left to shake in a conical tube with PBS for another 30 min before being loaded onto PDMS surfaces in imaging chambers. For both experiments, cells were left to adhere for 1 h after insertion into the imaging chamber, leading to a 6–7 h starvation period. Cell seeding concentrations were kept below 1×10^{-4} μm^{-2} to limit cell-cell interaction and enable study of the migration of individual cells.

Obstacle and flat PDMS surfaces

PDMS (Sylgard 184 Silicon Elastomer Kit, Dow Corning, Midland, Michigan) was mixed 1:10 resulting in a 1.72 MPa stiffness for all surfaces (19). Flat surfaces were prepared by spin-coated premixed PDMS onto polished Silicon wafers (Siegert Wafer, Aachen, Germany) and then baked for 4 h at 110°C. Before spin coating, wafers were silanized by trichloro(1H,1H,2H,2H-perfluorooctyl) silane deposition under vacuum (50 mbar) for 1 h to ensure proper PDMS detachment later. Before use, PDMS was cut, peeled off, and washed with ethanol (70%). For migration experiments, PDMS was cast around a 250–500 μm thickness; for limE-GFP imaging, PDMS was cast ultrathin (<50 μm) enabling 100× (working distance = 130 μm) imaging.

Pillar obstacle fields were prepared using a molding process. The pillar molds were prepared by two-photon direct laser writing using the Photonic Professional GT (Nanoscribe, Eggenstein-Leopoldshafen, Germany). First, a negative of the topotaxis pillar grids ($s = 0.01 - 0.03$, see pillars section) were designed using Inventor (Autodesk, Mill Valley, California) and, via a stereolithography format (.stl), imported to DeScribe (Nanoscribe) to prepare for direct laser writing. Then, two-photon cross-linking was performed using the IP-S resin (Nanoscribe) deposited on a silicon wafer. Different laser powers and scan speeds were chosen for bulk and edges of the structure, 27 and 42% (of 140 mW), 10 and 40 mm/min, respectively. To remove excess resin, molds were developed for 45 min in polyglycidylmethacrylate. After blow drying with nitrogen, wafers were silanized as described previously. To produce the pillar field casts, PDMS was deposited over the wafer (with mold on top), baked, cut, peeled off, and washed with ethanol (70%).

PDMS inserts were hydrophilicitized by 15 min of UV/ozone exposure (UVO-42, Jelight, Irvine, California) and placed inside an imaging slide (0.8 sticky-Slide I Luer, Ibidi, Gräfelfing, Germany), to be used immediately. Before loading cell suspensions, imaging slides were washed with ethanol and then PBS. To determine the quality of the mold and PDMS inserts, a cast of each pillar design was imaged using a nanoSEM (FEI/Thermo Fisher Scientific, Eindhoven, the Netherlands) scanning electron microscope (SEM). Samples were imaged at 10 kV, with a spot size of 4.0. Before imaging, PDMS structures were coated with 2–8 nm Pt/Pa using a plasma magnetron sputter coater (208HR, Cressington, Watford, UK) to enhance conductance.

Live-cell imaging and tracking

Cells were imaged every 8–10 s for experiments on flat PDMS and every 20 s for topotaxis assays. Measurements lasted for 1–3 h and were performed with either 10× or 20× air objectives (Plan Fluor, Nikon, Tokyo, Japan) on a Nikon Eclipse Ti microscope equipped with a confocal spinning disk unit operated at 10,000 rpm (Yokogawa, Tokyo, Japan). The cytoplasmic GFP was excited at 488 nm using a solid-state diode laser (Coherent, Santa Clara, California) supported in an Agilent MLC4 unit (Agilent Technologies, Santa Clara, California), at reduced intensity (25% of 2.4 mW) controlled by an Acousto-Optic Tunable Filter. Emission was filtered by a quad-band fluorescence filter (TR-F440-521-607-700, IDEX LLC, Rochester, NY). Images were captured using an exposure time of 200 ms by an Andor iXon Ultra 897 High Speed EM-CCD camera (Andor Technology, Belfast, UK). Images of higher magnification were produced with the same setup but using different objectives: Fig. 1 *E* with 40× air (Plan Fluor, Nikon), limE-GFP; Figs. 1 *D* and 2 *A* with 60× water (Plan Apo VC, Nikon); Figs. S1 *C* and A1 *A* with 100× oil (CFI Plan Apo, Nikon).

Image tracking was performed using ImageJ (http://imagej.nih.gov/ij/). Microscopy time-lapse images were contrast and brightness adjusted, and run through a Gaussian filter ($\sigma = 2$) to enable optimal cell body recognition. The ImageJ plugin CellEvaluator was used to determine the x, y-coordinates of the center-of-mass of each cell body in each frame (21). By linking all these x, y-positions together, cell trajectories were obtained.

Empirical measurement of cell area

Fluorescence microscopy images of cell migration experiments on flat PDMS were used to fit the cell surface area (A_σ) parameter in the CPM. Frames used for area analysis were chosen sufficiently far apart ($f^{-1} = \delta t = 200$ s) to avoid correlations. The two-dimensional (2D) projection of the cell body was determined using Sobel edge detection, applied to cytoplasmic GFP images obtained using the 20× air objective (0.657 μm/pix). Brightness and contrast were adjusted to rescale pixel intensities (i.e., only using the range of 16-bit intensities of GFP signal detected). Image analysis was performed using MATLAB, and the Image Processing Toolbox (MATLAB v.2019a, The MathWorks, Natick, MA) in particular. First, edges were detected (Sobel) using an appropriate threshold, then the resulting binary edge image was dilated, holes were filled, borders

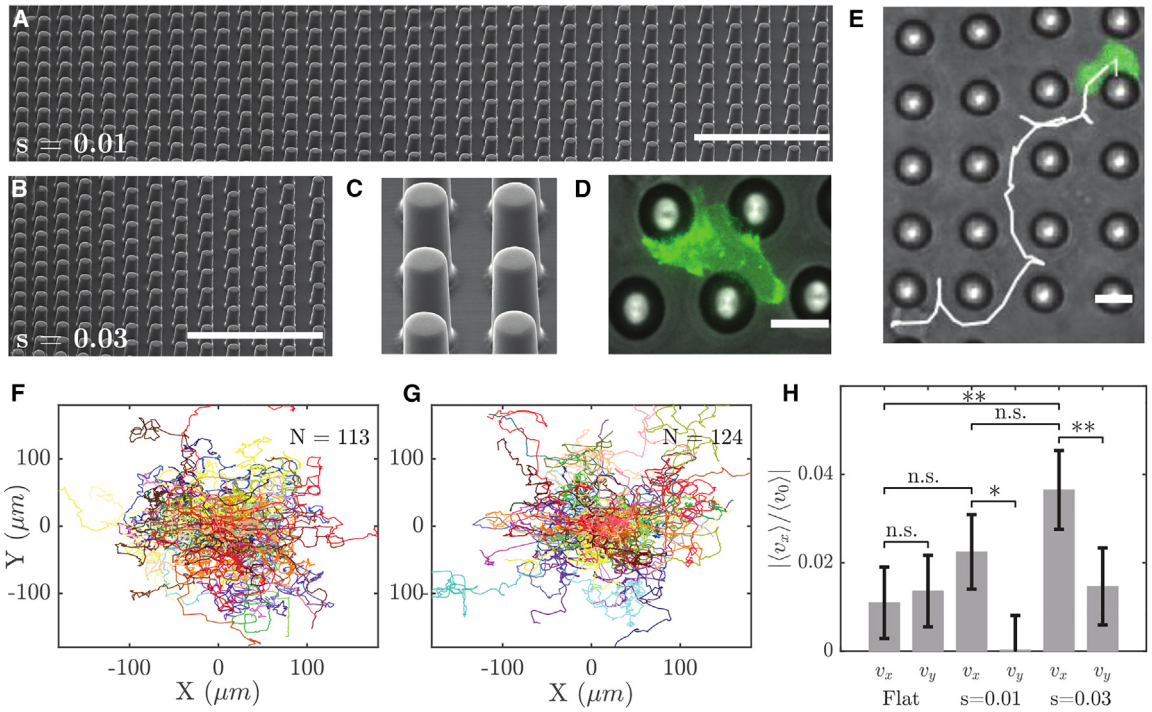

FIGURE 1 Large-scale topotaxis for highly motile ameboid cell migration (*D. discoideum*). (*A*) SEM micrograph of the $s = 0.01$ pillar field. Scale bar, 100 μm. (*B*) Same micrograph, but for $s = 0.03$. (*C*) Detailed micrograph of pillars ($h = 20$ μm, $d = 10$ μm). (*D*) Actin polymerization hotspots visualized for a cell migrating through a pillar field. Fluorescence is LimE-GFP expressed in LimE null cells (18,20) after z-projection. Scale bar, 10 μm. See also Video S1. (*E*) Bright-field image of a pillar field ($s = 0.03$) overlaid with the trajectory of a migrating starved *D. discoideum* cell (free cytoplasmic GFP in *green*). Scale bar, 10 μm. (*F*) Trajectory plot of 113 cells moving on the topotaxis field $s = 0.01$ during 4 independent measurements. (*G*) Trajectory plot of 124 cells moving on topotaxis field $s = 0.03$ during 4 independent measurements. (*H*) Comparison of the normalized mean drifts $\langle v_{x,y}\rangle / \langle v_0\rangle$ measured in all live cell experiments (flat, $s = 0.01$ and $s = 0.03$). The error bars are the 95% confidence intervals. During this analysis all randomly directed drift noise ($v_{x,\text{flat}}$ $v_{y,\text{all}}$) was reoriented along the positive axis to align any noise with the signal, and subject any bias in motion to the most rigorous significance test possible (see materials and methods and Fig. S2). The measured drift increases with an increase in the strength of the gradient s, as is demonstrated by increasing means. The underlying distributions are nonnormal (see Fig. S2, *B* and *C* for normality tests) and therefore the nonparametric Kruskal-Wallis test was used to perform an overall significance test ($p = 0.0024$) over the v_x and v_y values. A post hoc Dunn's test shows that the topotaxis assays have a significant drift in the x, y directions, and the strongest gradient has a significantly higher drift than all other experimental configurations. The shallow gradient $s = 0.01$ is not significantly different compared with the flat and $s = 0.03$ configurations ($p_{\text{flat}} = 0.1, p_{s=0.03} = 0.3$) when all noise is directionally aligned. $^*p = 0.05$, $^{**}p = 0.01$.

cleared, and the image eroded (equal to the initial dilation). Then all groups of nonzero, adjacent pixels forming a cell were identified and properties (using *regionprops*), such as the area, extracted.

Models

ABP model

We use the ABP model as described previously by Schakenraad et al. (14). In this model, a particle is described as a disk of radius R_p at location $\mathbf{r}(t)$, with speed v_0 moving in the direction $\mathbf{p} = (\cos\theta, \sin\theta)$ which changes according to:

$$\frac{d\mathbf{r}}{dt} = v_0\mathbf{p} + \mu\mathbf{F} \tag{1}$$

$$\frac{d\theta}{dt} = \sqrt{2D_r}\xi, \tag{2}$$

with μ a mobility coefficient, $\mathbf{F} = \mathbf{F}(\mathbf{r})$ the interaction force between particle and obstacle, $\xi = \xi(t)$ a random variable with zero mean and time correlation $\langle\xi(t)\xi(t')\rangle = \delta(t - t')$. The rotational diffusion coefficient $D_r = 1/\tau_p$ is the inverse of the persistence time τ_p of the ABP. The interaction force $\mathbf{F}$ is given by

$$\mathbf{F} = \begin{cases} -\dfrac{v_0}{\mu}(\mathbf{p}\cdot\mathbf{N})\mathbf{N}, & \text{if } |\Delta\mathbf{r}_0| \le R \\ 0, & \text{otherwise,} \end{cases} \tag{3}$$

with $\mathbf{N}$ a unit vector normal to the obstacle surface, $|\Delta\mathbf{r}_0|$ the distance between the centers of the particle and the obstacle, and R the effective particle radius as the sum of the particle and pillar radius $R = R_p + R_0$. In our simulations $\mu = 1$, and v_0 and τ_p are set to experimentally determined cell speeds and persistence times. $R_p = 1$ μm by default, to represent the size of the nucleus of *D. discoideum* (22,23), or is set to 0 μm (no volume) or 1.8 μm, which is the maximal possible radius to fit through the smallest distance in the topotaxis grid.

CPM of persistently moving cells

We use the 2D CPM (24) with either of two extensions for modeling persistent cell movement (see sections Act-CPM and ABP-CPM). The CPM represent cells on a regular square lattice $\Lambda \subset \mathbb{Z}^2$. Each lattice site, $\vec{q} \in \Lambda$, is associated with a spin value $\sigma(\vec{q}) \in \{1, 0, -2\}$, that assigns the lattice

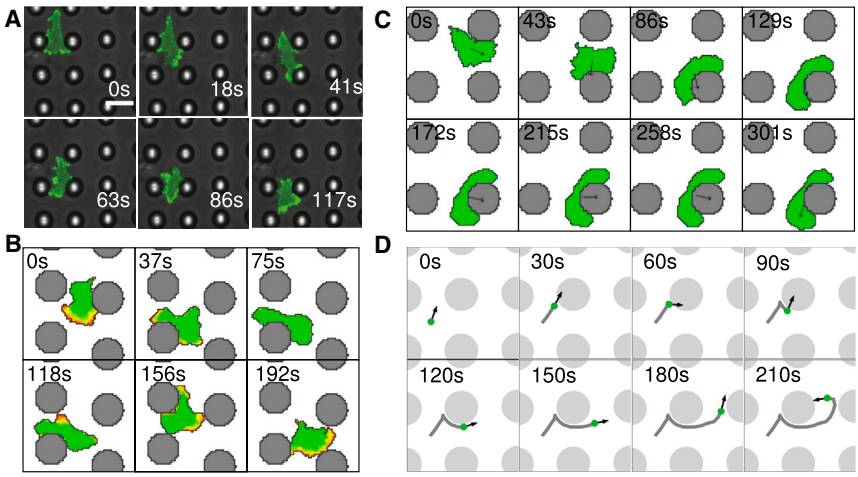

FIGURE 2 Examples of frontal collision with a pillar of in-vitro-starved *D. discoideum* and simulations. (*A*) Starved *D. discoideum* navigating through a topotaxis assay. The degree of actin polymerization (*green*) is visualized through fluorescence of LimE-GFP. (*B*) Act-CPM simulation: Act levels are colored from red ($Act(\vec{q}) = \mathrm{Max}_{Act}$) to green ($Act(\vec{q}) = 0$). Once the polarized cell hits the pillar, it loses its polarization, a new Act front appears, and the cell polarizes again and moves away from the pillar. (*C*) ABP-CPM simulation: the arrow is the preferential direction vector **p** of the cell, starting at its center of mass. Once the cell collides with the pillar, it can only move away once **p** points away from the pillar (final frame). (*D*) ABP model simulation: the black arrow is the particle's directional vector **p**, the gray line displays the particle's trajectory. For particles colliding with a pillar, the displacement's component normal to the pillar surface is lost, resulting in motion away from the pillar only when **p** has shifted away from the pillar. See also Videos S1 and S4.

site to the cell ($\sigma(\vec{q}) = 1$), the medium ($\sigma(\vec{q}) = 0$), or a pillar ($\sigma(\vec{q}) = -2$). The cell is represented as the collection of lattice sites marked with $\sigma = 1$: i.e., $\{\vec{q} \in \Lambda, |, \sigma(\vec{q}) = 1\}$.

Cell motion is modeled by updating the lattice through iterative attempts to extend or retract the cell into neighboring lattice sites. For a copy attempt, the algorithm selects at random a lattice site $\vec{q}$ and one of its eight neighbors $\vec{q'}$. If $\sigma(\vec{q}) \neq \sigma(\vec{q'})$, the algorithm computes $\Delta\mathcal{H}_{\mathrm{total}}$, the change in Hamiltonian together with the energy change due to active forces from the cell's persistence, which determines the success of a copy attempt. The Hamiltonian $\mathcal{H}$ balances the forces of cell-medium and cell-pillar interactions, and cell area and cell perimeter constraints (25):

$$\mathcal{H} = \sum_{\vec{u},\vec{v}} J_{\sigma(\vec{u}),\sigma(\vec{v})}\left(1 - \delta_{\sigma(\vec{u}),\sigma(\vec{v})}\right) + \lambda_{\mathrm{area}}(a_\sigma - A_\sigma)^2 + \lambda_{\mathrm{perimeter}}(p_\sigma - P_\sigma)^2 \quad (4)$$

Here, $J_{\sigma(\vec{u}),\sigma(\vec{v})}$ describes the adhesion energy between two neighboring lattice sites $\vec{u}, \vec{v}$ of types $\sigma(\vec{u}) \neq \sigma(\vec{v})$. We set $J_{\mathrm{pillar,medium}} = 0$ to only take the adhesion energy between cell and medium ($J_{\mathrm{cell,medium}} = 20$ (17)) or cell and pillar ($J_{cell,pillar}$, varies) into account. The second and third Hamiltonian term describes the area and perimeter constraint and penalize deviation of the cell area a_σ from its target area A_σ and of cell perimeter p_σ from the target perimeter P_σ. The λ values indicate the weight of both constraints.

The probability of a successful copy attempt depends on $\Delta\mathcal{H}$ and an extension-specific $\Delta\mathcal{H}_{\mathrm{motility}}$ (see subsections Act-CPM and ABP-CPM) via $\Delta\mathcal{H}_{\mathrm{total}} = \Delta\mathcal{H} - \Delta\mathcal{H}_{\mathrm{motility}}$:

$$P(\Delta\mathcal{H}_{\mathrm{total}}) = \begin{cases} 1 & \text{if } \Delta\mathcal{H}_{\mathrm{total}} < 0 \\ e^{-(\Delta\mathcal{H}_{\mathrm{total}}/T)} & \text{if } \Delta\mathcal{H}_{\mathrm{total}} \geq 0 \end{cases},$$

with T denoting the noise in the system that allows for energetically unfavorable copy attempts to be accepted. Model time is expressed in Monte Carlo steps (MCSs). Within a single MCS, the expectation is that, for each lattice site, an update has been attempted once. Since we model only a single cell in a large field, many neighboring lattice site pairs will not lead to cell movement. We ignore such unfruitful copy attempts by using a rejection-free algorithm to speed up simulations (26,27).

Act-CPM. To model persistent cells, we use two different extensions of the CPM. First, we use the Act-CPM (17). It models the actin polymerization-driven persistent cell motility (17). Each lattice site $\vec{q}$ has an extra value, $Act(\vec{q})$, which can range from 0 to $\mathrm{Max}_{\mathrm{Act}}$ inside the cell. The *Act* value outside the cell is always 0. If the cell has recently made an extension into $\vec{q}$, $Act(\vec{q})$ is set to $\mathrm{Max}_{\mathrm{Act}}$. For every MCS, each nonzero *Act* value will be decreased by 1, until 0.

For the Act-CPM, $\Delta\mathcal{H}_{\mathrm{motility}} = \Delta\mathcal{H}_{Act}$. In a copy attempt extending the cell from a lattice site $\vec{c}$ into an empty lattice site $\vec{m}$, we look at the geometric mean of the *Act* values in $\mathrm{NB}(\vec{c})$, the Moore neighbors of $\vec{c}$ that are also within the cell, such that:

$$\Delta\mathcal{H}_{Act}(\vec{c} \to \vec{m}) = \frac{\lambda_{Act}}{\mathrm{Max}_{Act}}\left(\prod_{\vec{y} \in \mathrm{NB}(\vec{c})} Act(\vec{y})\right)^{\frac{1}{|\mathrm{NB}(\vec{c})|}}. \quad (5)$$

For retraction attempts, the sign changes, so $\Delta\mathcal{H}_{Act}(\vec{m} \to \vec{c}) = -\Delta\mathcal{H}_{Act}(\vec{c} \to \vec{m})$. As a consequence, the cell is more likely to extend outwards at areas with high *Act* values and is less likely to retract from such areas. This simulates the polarized actin structure of a cell in a phenomenological way. The two parameters λ_{Act} and $\mathrm{Max}_{\mathrm{Act}}$ can be tuned to obtain different cell motilities.

ABP-CPM. The ABP-CPM is a hybrid method between a CPM model extension (28) and the ABP model (14). Like the ABP model, the cell has a direction $\mathbf{p} = (\cos\theta, \sin\theta)$. Cell movement along this direction is favored. For each copy attempt extending the cell, the angle α between the resulting displacement of the center of mass and **p** is computed, and results in $\Delta\mathcal{H}_{\mathrm{motility}} = \Delta\mathcal{H}_{\mathrm{persistence}}$ like in (28):

$$\Delta\mathcal{H}_{\mathrm{persistence}} = \lambda_{\mathrm{persistence}} \cdot \cos(\alpha). \quad (6)$$

For updating θ, we use the same differential equation as in (14) (see Eq. 2):

$$\frac{d\theta}{dt} = \sqrt{\frac{2}{\tau_p}}\xi(t). \quad (7)$$

Here, τ_p stands for the persistence time, and $\xi(t)$ is a stochastic white noise term, modeled by a Gaussian distribution with mean 0 and variance $\sigma^2 = 2\frac{\Delta t}{\tau_p}$. The term Δt couples the time of Eq. 7 to the MCS, and we choose $\Delta t = 0.1\tau_p$. At initialization, the cell is assigned a θ from a uniform random distribution. We update θ each MCS. Different cell motilities can be obtained by tuning the parameters τ_p and $\lambda_{\mathrm{persistence}}$.

Pillars

We utilize two different pillar grids: a regularly spaced pillar grid and a pillar grid with a topotaxis gradient. The regularly spaced grids are defined by the distance between pillar centers d and the pillar radius R. The topotaxis grid is defined as by Schakenraad et al. (14). It consists of three different parts: a regularly spaced part on the left of the field, a part with a gradient in pillar distance in the middle, and another regularly spaced part on the right. The pillar gradient in the middle is defined by the following set of pillar centers P,

$$P = \left\{ (x,y) \in \mathbb{R}^2 \;\middle|\; \begin{array}{ll} x = \dfrac{d}{1-e^{-s}}(e^{sn}-1) + \dfrac{d}{2} & \text{and} \\ y = d\left(m+\dfrac{1}{2}\right)e^{sn}, & \text{with } n,m \in \mathbb{Z} \end{array} \right\}, \tag{8}$$

where d is the distance between pillar centers at the origin $(0,0)$, the center of the field. This gives a gradient in the horizontal axis with parameter s defining the steepness. The two regularly spaced grids at the left and right of the gradient part of the grid with respective pillar spacings $d_{\min}$ and $d_{\max} = 2d - d_{\min}$ limit the gaps between pillars to get too small or too big. Table 1 gives an overview of all grid measurements.

In the CPM, a lattice site $\vec{x}$ is assigned to a pillar if it is within a distance R from one of the pillar centers. Pillar lattice sites have $\sigma = -2$, so as not to be confused with the σ values of the medium or cells. As pillars are static, copy attempts into a pillar site are not allowed. However, copy attempts from a pillar site into a cell site $\vec{q}$ are allowed, although, in this case, not $\sigma(\vec{q}) = -2$ but $\sigma(\vec{q}) = 0$ is copied. This allows the cells to retract from the pillars and can be seen as medium flowing back in between cell and pillar from the third dimension, which we do not model explicitly. The interaction energy $J_{\text{cell,pillar}}$ can be adjusted to represent adhesive or repulsive pillar surfaces. In this work, $J_{\text{cell,pillar}} = J_{\text{cell,medium}}$, such that pillar adhesion is neutral in respect to adhesion to the medium, unless stated otherwise.

Establishing baseline motility

To quantitatively compare the topotaxis of simulated cells to *D. discoideum* cells, we tried to find parameters such that the simulated cells behave the same as the starved and vegetative *D. discoideum* cells on a flat PDMS surface without any pillars (Figs. S1 and A1). For the ABP model, we set v_0 and τ_p directly to the experimentally determined values (see trajectory analysis). For the CPMs, we changed the motility parameters λ_{Act} and Max_{Act}, and $\lambda_{\text{persistence}}$ and τ_p, to fit to the experimental data.

The experimental data used for fitting the motility parameters are: the surface area, instantaneous speed, effective diffusion coefficient, and persistence time. The surface area and speed were used to determine the length and timescale of the CPMs. The effective diffusion coefficient and persistence time had equal weights in our least-squares objective. Using a hill-climbing algorithm with multiple restarts, we obtained a shortlist of possible parameter values. The 15 best parameter sets were then scored 10 more times to obtain the best parameter set. The resulting effective diffusion coefficients and persistence times are shown in Tables 2 and A1. The optimal parameters are shown in Tables 3 and A2, and were used for further simulations.

TABLE 1 Pillar gradient grid parameter values for the experimental and simulation setup

		Experiment	CPM	
Symbol	Description	(μm)	(px)	(μm)
R	pillar radius	5	10	5.3
h	pillar height	18 ± 2	N/A	
d	pillar center distance at origin	16.8	32	16.8
$d_{\min}$	pillar center distance left cap	13.6	26	13.7
$d_{\max}$	pillar center distance right cap	19.9	38	20.0
s	gradient steepness	0.01, 0.03	0.01–0.09	

Trajectory analysis

Cell trajectories recorded on flat and pillar PDMS surfaces were analyzed with an in-house MATLAB code (v.2019b). The instantaneous velocities v, persistence times τ, and diffusion constants D extracted for the flat trajectory data by this analysis were used to calibrate the CPMs and ABP simulations. Dying or otherwise immotile cells (see (12)) and insufficiently long trajectories (flat $n < 100$, topotaxis $n < 30$) were discarded for analysis, to prevent noise in mean-squared displacement (MSD) values at long lag times.

The displacement of the cell between frames was found by $\overline{r}(t) = \overline{R}(t+\Delta T) - \overline{R}(t)$, where $\overline{R}(t)$ are the vectors described by the x,y-coordinates of the cell center in each image. The instantaneous velocity of each cell was estimated using the time-averaged velocity between frames,

$$\langle v(\Delta T)\rangle_{\text{T}} = \frac{1}{n-1}\sum_{k=1}^{n-1}\frac{|\overline{R}(t_k) - \overline{R}(t_k - \Delta T)|}{\Delta T}. \tag{9}$$

Here, the trajectory time t_k is discretized by the constant frame rate of the camera, $t_k = k\cdot\Delta T$, with $k = 0,\ldots,n$, $\Delta T = 10$ s or 20 s, and where n is the number of frames in a trajectory. The ensemble average of each experiment (and simulation) was obtained by taking the mean of all v per experiment. For the experimental trajectories, the time-averaged MSD was used:

$$\langle \Delta\overline{r}^2(t_{\text{lag}})\rangle_{\text{T}} = \frac{1}{n-m}\sum_{k=1}^{n-m}\left(\overline{R}(t_k + t_{\text{lag}}) - \overline{R}(t_k)\right)^2. \tag{10}$$

In this expression, m represents the lag time multiple under consideration $t_{\text{lag}} = m\Delta T$. The time-averaged MSDs were averaged over all N trajectories per lag time, and subsequently fit to Fürth's formula,

$$\text{MSD}(t) = 2v_0^2\tau t - 2v_0^2\tau^2\left(1 - e^{-t/\tau}\right). \tag{11}$$

From this fit the characteristic persistence times (τ) and effective diffusion constants (D_{eff}) for both vegetative and starved *D. discoideum* cells moving on flat PDMS were extracted and used to fit the CPMs and ABP model.

To determine the persistence time in the simulation, we computed the ensemble-averaged MSD of $N = 1000$ simulated cells (CPMs) or $N = 10,000$ particles (ABP model):

$$\langle r(t)^2\rangle = \frac{1}{N}\sum_{i=1}^{N}\left(\overline{R}(t_0+t) - \overline{R}(t_0)\right)^2. \tag{12}$$

TABLE 2 Cell motility properties for starved *D. discoideum* on a flat PDMS surface, the resulting properties for the ABP simulations, and best fits for the Act-CPM and ABP-CPM

	Experimental	ABP	Act-CPM	ABP-CPM
Length equivalent 1 px (μm)	–	–	0.525	0.525
Time equivalent 1 MCS (s)	–	–	0.373	0.574
Speed (μm/s)	0.197 ± 0.001	0.193 ± 0.000	–	–
Area (μm^2)	110.4 ± 45.1	–	–	–
Effective diffusion (μm^2/s)	1.82 ± 0.68	1.77 ± 0.04	1.76 ± 0.08	1.87 ± 0.08
Persistence time (s)	91.98 ± 0.98	92.0 ± 1.7	89.30 ± 2.22	89.89 ± 3.33

Here, $t_0 = 0$ for the ABP simulations and $t_0 = 120$ MCS for both CPMs to allow for an initialization period for the Act-CPM. We then fitted to $\langle r(t)^2 \rangle$ Fürth's formula (Eq. 11) for the ABP trajectories, or the adapted Fürth's formula for the CPM trajectories

$$\mathrm{MSD}(t) = 4D_T t + 2v_0^2\tau t - 2v_0^2\tau^2\left(1 - e^{-t/\tau}\right), \quad (13)$$

which describes the MSD of a persistent random walk with translational noise (29). Here, τ is the persistence time, v_0 the constant speed, and D_T is the translational diffusion caused by thermally induced fluctuation, which is inherent in the CPM. The corresponding effective diffusion constants are described by $D_{\mathrm{eff}} = \frac{1}{2}v_0^2\tau$ (ABP) or $D_{\mathrm{eff}} = D_T + \frac{1}{2}v_0^2\tau$ (CPMs). However, we obtained D_{eff} independently from Eq. 13 by fitting the MSD of a Brownian particle

$$\mathrm{MSD}(t) = 4D_{\mathrm{eff}}t, \quad (14)$$

to Eq. 12 for $t \geq 2000$ MCS (CPMs) or $t \geq 900$ s (ABP):

For flat and topotaxis assays of the experimental and simulated trajectories, migratory drift ($v_{x,y}$) was calculated by averaging over all displacements of all trajectories,

$$\langle v_{x,y} \rangle = \frac{1}{n-1}\sum_{i=1}^{n-1}\left(\overline{R}(t_i + \delta t) - \overline{R}(t_i)\right) \quad (15)$$

where n is the total number of displacements measured. For the simulated topotaxis assays, we performed 1000 single-cell CPM simulations or 10,000 ABP model simulations for each parameter setting. To measure topotactic drift v_x we computed the mean velocity in the x-direction with Eq. 15, using the equivalent of $\delta t = 20$ s intervals for all cell or particle tracks, and n all time steps in which the cell or particle was in the gradient part of the pillar grid. To subject the measured drift distributions (Eq. 15) to the most rigorous statistical evaluation possible, each randomly oriented noise expected in the isotropic directions (v_{flat} and v_y) was oriented along the direction of expected drift $+x$ during analysis. After the live-cell measured drift distributions were found to be nonnormal by Kolmogorov-Smirnov and Lelliefors testing, the Kruskal-Wallis test by ranks ($\alpha = 0.05$) was used to determine whether samples originated from different distributions. To determine pairwise statistical significance, a post hoc Dunn's test was used on independent groups (either v_x or $v_y$values).

TABLE 3 Parameter values of the best fits for the starved *Dictyostelium* cells for both the Act-CPM and ABP-CPM

Parameter	Starved
T	20
A_σ	400
λ_{area}	50
P_σ	313
$\lambda_{\mathrm{perimeter}}$	1
$J_{\mathrm{cell,medium}}$	20
	Act-CPM
λ_{Act}	129
$\mathrm{Max}_{\mathrm{Act}}$	37
	ABP-CPM
$\lambda_{\mathrm{persistence}}$	159
τ_{p}	30

RESULTS

Starved *D. discoideum* cells show topotactic drift increasing with gradient steepness

Before investigating the physical origin of topotaxis through multiple in silico models, topotactic drift was first experimentally (re)confirmed in square pillar lattices with a continuously changing pillar density. Although earlier work already focused on long-range topotactic drift for ameboid motility in fields of anisotropically placed cell-sized obstacles, the drift in these experiments was measured on trigonally arranged pillar fields with a discontinuous gradient (12) instead of a square lattice with a continuous gradient. The square pillar lattice with a continuous gradient was later introduced in (14), and provides a more well-defined approach to studying gradient-dependent differences in topotactic response. Contrary to using experimental data from previous experiments, measuring cell migration on the same lattices used for modeling topotaxis ensures a more optimal comparison between experimental and simulated data. Fig. 1 *A–C* shows SEM micrographs of the new square PDMS pillar grids used for cell motility experiments here, which were produced using soft photolithography techniques similar to earlier work (see materials and methods for details). The pillars were placed according to Eq. 8, as introduced in (14), and their overall design parameters are shown in Table 1.

The $s = 0.01$ and $s = 0.03$ gradient pillar fields (see Fig. 1 *A* and *B*) were chosen as suitable benchmarks for measuring the topotactic response of starved *D. discoideum* on the new pillar gradients. Measuring topotaxis on steeper gradients ($s > 0.03$) was found to be experimentally unfeasible, as these grids produce few and short trajectories in combination with sparse cell seeding, and very gradual gradients ($s \ll 0.01$) are expected to result in low drifts, possibly within experimental error. The cells navigated smoothly between the pillar obstacles (Figs. 1 *D*, *E*, and 2 *A*; Video S1) during migration experiments (0–3 h). Cell movement was imaged using fluorescent confocal microscopy and tracked using image analysis (Fig. 1 *E*, also see live-cell imaging and tracking). The experiments yielded more than 100

trajectories per pillar gradient, plotted centered in Fig. 1, *F* and *G*. To analyze long-range topotaxis of the cells, the drift of the cell center in both the *x* and *y* direction (v_x and v_y) was calculated from cell tracks in the gradient (Fig. 1 *H* and Eq. 15). To subject the measured drift in the anisotropic assays to the most rigorous evaluation with respect to the experimental noise, the randomly directed drifts (flat and v_y) were aligned with the direction of the spatial gradient $+x$ before any significance testing during analysis. The cell trajectories have a significant drift in the positive *x* direction (i.e., toward sparser pillar densities) for both pillar gradients compared with the corresponding v_y in the gradient. In addition, the mean drift increases with gradient steepness *s*, and although only the steepest gradient yields a significantly different drift with respect to all other orientations, the $s = 0.01$ drift is significant to all other directions for randomly oriented noise (as seen by using the raw data, see Fig. S2).

The fluorescence time-lapse microscopy of starved *D. discoideum* migrating on flat PDMS served as a control for the topotaxis data, but also served as the baseline data necessary to empirically calibrate the input parameters required for CPM simulations. The motility of the cells on flat PDMS (Fig. S1 and Video S2) yielded the base mean cell area (Fig. S1 *D*), mean speed (Fig. S1 *E*), persistence time (Fig. S1 *G*), and diffusion constant (Fig. S1 *H*), summarized in Table 2, necessary as initial input to generate CPM trajectories. In general, the experimental data show that starved *D. discoideum* cells are highly motile compared with other cell types (30), and move persistently randomly with a relatively similar speed and persistence time across the cell population for long measurement times (31). The cell area and perimeter are equally similar over time and population, even though the cells continuously grow and retract pseudopods (see Fig. S1 and (32)).

The ABP, Act-CPM, and ABP-CPM simulations applied in this study require different sets of input parameters. ABPs are fully defined by a constant speed v_0 and persistence time τ_p, whereas CPM simulations require an input target cell area A_σ, cell perimeter P_σ, and to set the persistence parameters λ and Max_{Act} or τ_p, need an input diffusion constant *D* and persistence time τ_p to calibrate motility. Furthermore, the time and spatial resolution of the CPM system was set by comparing the typical cell area and speed of *D. discoideum* with the time and length scale of MCS simulations (see Table 2 for possibilities). In silico cell motion was fit to represent experimental motion by weighing up observables extracted from simulated trajectories to those gathered from experimental trajectories (via the same procedures, i.e., equal frame rate and computational method). The ABP simulations were simply set by using the experimentally determined mean cell speed and persistence time, which resulted in only slightly slower and less-diffusive motion (Table 2). In the case of CPM simulations, however, the observables were compared through a fitting procedure (see models for details) to obtain a best match to experimental motility. The MCS parameter values used for Act-CPM (λ_{Act} and $\mathrm{Max}_{\mathrm{Act}}$) and ABP-CPM ($\lambda_{\mathrm{persistence}}$ and τ_p) are shown in Table 3, with the corresponding motility properties shown in Table 2. See Video S3 for example, simulations of both systems on a flat substrate. Overall, the data summarized in Table 2 indicate that we achieved a close match between simulated and experimental trajectory observables for all three models on flat surfaces.

Method of persistence affects topotactic capacity of cells

After confirming topotactic drift in square pillar grids with a continuous spatial gradient, and calibrating the simulations of persistent random cell motion with experimental data, we turned to an extensive in silico investigation of cell-sized obstacle topotaxis. Fig. 2 summarizes how the various simulated cell bodies respond to obstacles and provides comparison with a representative cell-pillar interaction of starved *D. discoideum*. The ameba has a single actin front before interacting with a pillar (*green*, Fig. 2 *A*, 0–18 s), which splits into two upon collision (Fig. 2 *A*, 18–41 s). One of the two newly formed actin fronts becomes the dominant side during the collision, which then guides the entire cell body around the pillar (Fig. 2 *A*, 63–117 s). The Act-CPM cell-pillar interaction follows a similar, CIL-like mechanism of navigating around obstacles (Fig. 2 *B*). After colliding with a pillar, the cell temporarily loses actin polarization (Fig. 2 *B*, 75 s), and then repolarizes in a new direction (Fig. 2 *B*, 118–192 s). The ABP-CPM and ABP pillar collisions develop very differently, as these cells or particles always propagate via a self-dictated desired direction of motion; therefore, pillar interactions never alter their (inherent) persistence (Fig. 2, *C* and *D*). For these models, the pillars act as areas of excluded volume, unable to alter intrinsic persistence, and only guide the cells around the pillar wall through the velocity component of the cell that does not point directly at the pillar center. The two ABP simulations react differently to the same method of unaltered persistence. The ABP particles always remain in motion, gliding past pillar walls (Fig. 2 *D*, 90–150 s), whereas the inclusion of a cell body for ABP-CPM can lead to prolonged stationary states through cell-pillar embraces. Moreover, the ABP-CPM cells remain longer in contact with the pillar and rotate further around the pillar than the Act-CPM cells (Fig. S6).

Example trajectories of ABP- and Act-CPM simulations are shown in Fig. 3, *A–F* (Video S4) for three different gradients. Act-CPM trajectories (Fig. 3, *A–C*) do not penetrate the dense side of the grid as much as ABP-CPM cells (Fig. 3, *D–F*). The mean population displacements ($\langle x(t)\rangle$ and $\langle y(t)\rangle$, Fig. 3, *G* and *H*) show that there is drift along the *x* axis for all gradient steepness (*s*), indicating that the simulated cells perform topotaxis in both models.

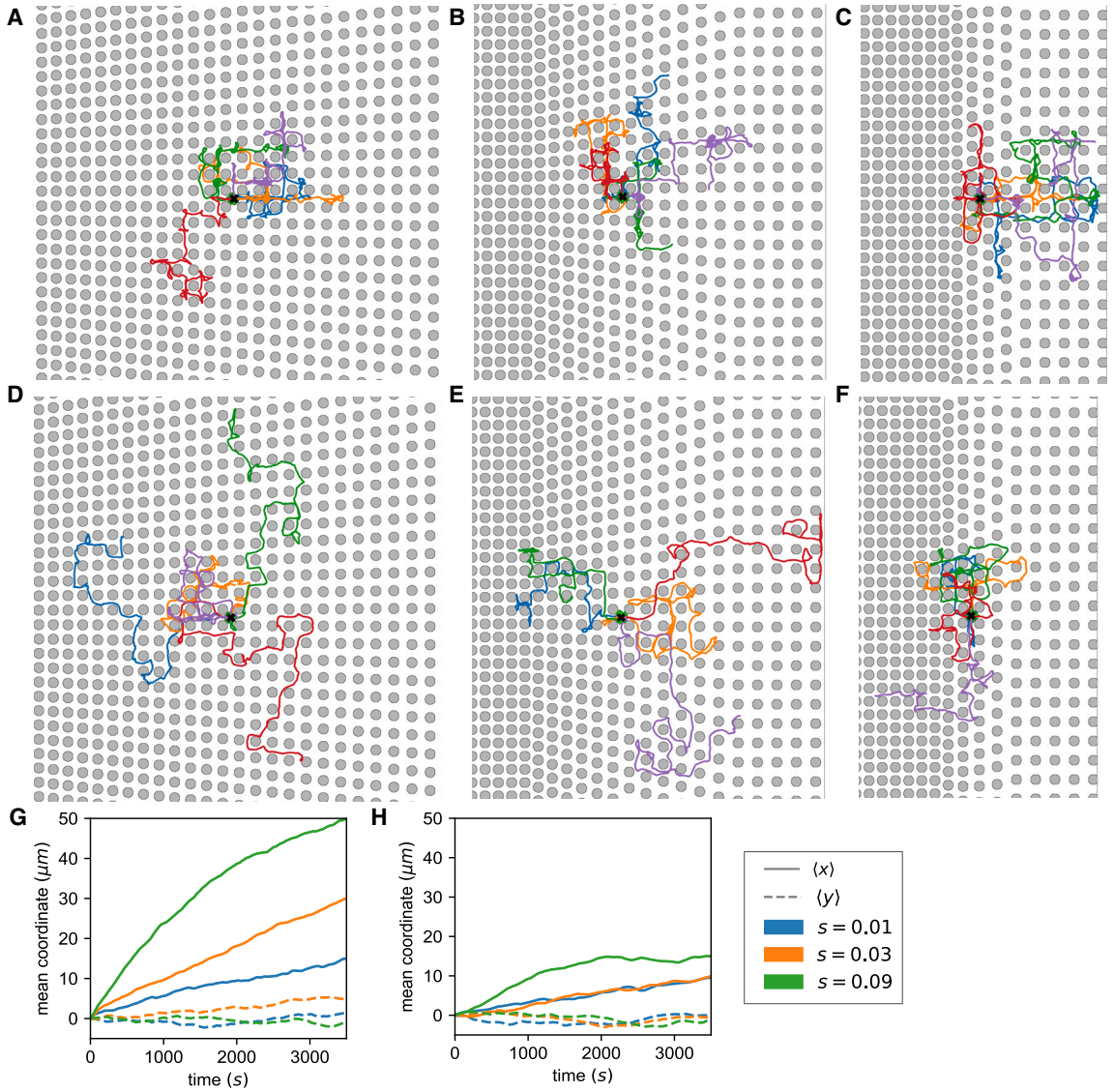

FIGURE 3 Trajectories of starved simulated cells and means of x and y coordinates over time for different gradient steepness parameter (s) values. (*Top row*) Act-CPM example trajectories: (*A*) $s = 0.01$, (*B*) $s = 0.03$, (*C*) $s = 0.09$. (*Middle row*) ABP-CPM examples: (*D*) $s = 0.01$, (*E*) $s = 0.03$, (*F*) $s = 0.09$. Starting location is marked with a black cross and the depiction of a cell. Each trajectory has its own color. (*Bottom row*) Mean x and y coordinates over time for gradient steepness s corresponding to the gradients shown in the rows above. (*G*) Act-CPM. (*H*) ABP-CPM.

Compared with the fully controllable simulations, the in vitro experiments come with additional challenges, such as random cell seeding, population heterogeneity, and variations in recorded trajectory durations. Therefore, comparisons between the two systems are best made using time and population averages (Fig. 4, *A–C*). The drift velocity in the direction of the gradient (v_x, Fig. 4 *A*) increases as a function of steepness for the trajectories of both the experimental data and all models. The models have a mean drift proportional to the gradient steepness, as described for ABPs by Schakenraad et al. (14), but there is a clear difference between the ABP and CPM simulations: CPMs show a higher increase in drift than the ABP model and, furthermore, the Act-CPM is most effective at performing topotaxis. When directly comparing the topotactic drift between simulations and *D. discoideum*, the ABP-CPM predictions are closest to the experimental data, with Act-CPM drifting more, and the ABP model underestimating ameboid topotaxis. In the case of ABPs, there is a small effect of particle size on the topotactic drift ($R_p \in \{0, 1, 1.8\}$, see Fig. S3 for more details).

Directly comparing the unnormalized topotactic drift v_x assumes that the base motile response across all the investigated systems does not differ in a gradient versus on a flat substrate, or, for that matter, as a function of gradient steepness. However, earlier work by Schakenraad et al. suggest that this might not be the case. The mean instantaneous velocity $\langle |v_{ins}| \rangle$, an often used indicator of base cellular

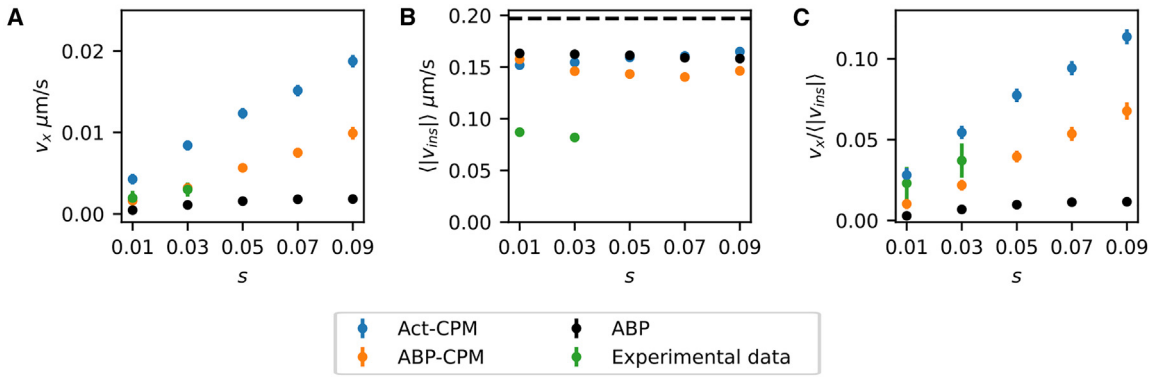

FIGURE 4 Topotactic drift and instantaneous speed of starved parameter set against gradient steepness s. Each orange or blue data point represent the average of 1000 simulations. Error bars indicate 97.5% confidence interval (CI). (*A*) Topotactic drift v_x. (*B*) Instantaneous speed $\langle|v_{ins}|\rangle$. The dotted line depicts the instantaneous speed of starved cells in the absence of pillars. (*C*) Relative topotactic drift $v_x/\langle|v_{ins}|\rangle$).

motility (33,34), is affected by pillar distance and, since cells in steeper gradient encounter different pillar distance more quickly, their instantaneous velocity can vary across different gradients. The $\langle|v_{ins}|\rangle$ is shown in Fig. 4 *B* for the experimental and simulated data, and develops differently for each model. The mean speed of ABPs, *D. discoideum*, and ABP-CPM cells drops with increasing gradient steepness, although at different rates, whereas the Act-CPM trajectories gain motility as a function of steepness. Overall, the instantaneous velocities always drop when compared with movement on flat substrates, but *D. discoideum* features a larger decrease in speed than the simulated cells. To properly compare the topotactic response across all the investigated systems, the drift must be normalized to the mean instantaneous velocity to account for the overall, dissimilar drop in motility on pillar substrates, and for any differences in speed response to varying the gradient steepness. Normalizing the topotactic drift ($v_x/\langle|v_{ins}|\rangle$, Fig. 4 *C*) increases the distinction between ABP and CPM cells, highlighting the influence of cellular volume on cell-sized obstacle topotaxis, and also positions the experimental topotactic response between the two CPM simulations.

Summarizing the in silico results so far, the inclusion of a dynamic cell body in the CPMs clearly influences the overall topotactic response, and provides a more accurate estimation of the topotactic drift measured for *D. discoideum* in vitro than ABP simulations. Especially the comparison between ABP and ABP-CPM highlights this finding, as the two models share the exact same method of generating persistence, but the pillar collisions ensue differently for ABP-CPM through the inclusion of a dynamic cell body, which seems to temporarily decrease motility during pillar interactions (Fig. 2). In the case of Act-CPM, the CIL-like pillar interaction may disrupt persistence (or motility) most, which seems to translate into the strongest topotactic drift. If cell-pillar interactions indeed cause different decreases in motility or persistence, this is important, as obstacle-induced disruptions of motion can lead to the emergence of topotaxis through the anisotropy in pillar density along the direction of the gradient. A positionally dependent difference in persistence leads to a net population drift in the direction of the gradient (see (14,16)). In the next section we investigate if the model with the strongest topotactic response, in this case Act-CPM cells, is indeed accompanied by the largest difference in obstacle-induced disruption of persistence or motility along the gradient axis.

Cell-pillar interactions are most disruptive for Act-CPM persistence

Inspired by Novikova et al. (16), Schakenraad et al. (14) attributed topotaxis to changes in effective persistence length $l_{\text{eff}} = v_{\text{eff}} \cdot \tau_{\text{eff}}$ as a function of position on the gradient axis. They argued that the increase in pillar density in the direction of the gradient leads to longer persistence lengths during movement, and therefore causes drift in the direction of the gradient. Here, we extend the results of Schakenraad et al. by calculating the same observables of persistent random motion for the Act-CPM and ABP-CPM systems that were previously determined for ABPs. First, the diffusion constant D_{eff} was calculated by a fit of the second moment of Brownian motion in two dimensions (Eq. 14) to the ensemble-averaged MSD (Eq. 12) of the trajectories at long lag times, i.e., during the diffusive regime of persistent random motion. Subsequently, the persistence time τ_{eff} was determined by fitting the full ensemble-averaged MSD to Fürth's equation for persistent random motion (Eq. 11 for the ABP model, and corrected for noise by an extra translational diffusion term for the CPMs, Eq. 13, see materials and methods). As a final step, the instantaneous velocities v_{eff} were measured by computing $\langle|v_{ins}|\rangle$ for each pillar configuration, and subsequently used to determine the associated persistence lengths (l_{eff}). In general, the data were well fit by the theoretical curves for Fürth and Brownian MSDs, with the exception of the recorded trajectories on the pillar grids with $d = 13.1$ μm, where the cell bodies were mostly stuck at their starting unit cell, leading to strong subdiffusive behavior.

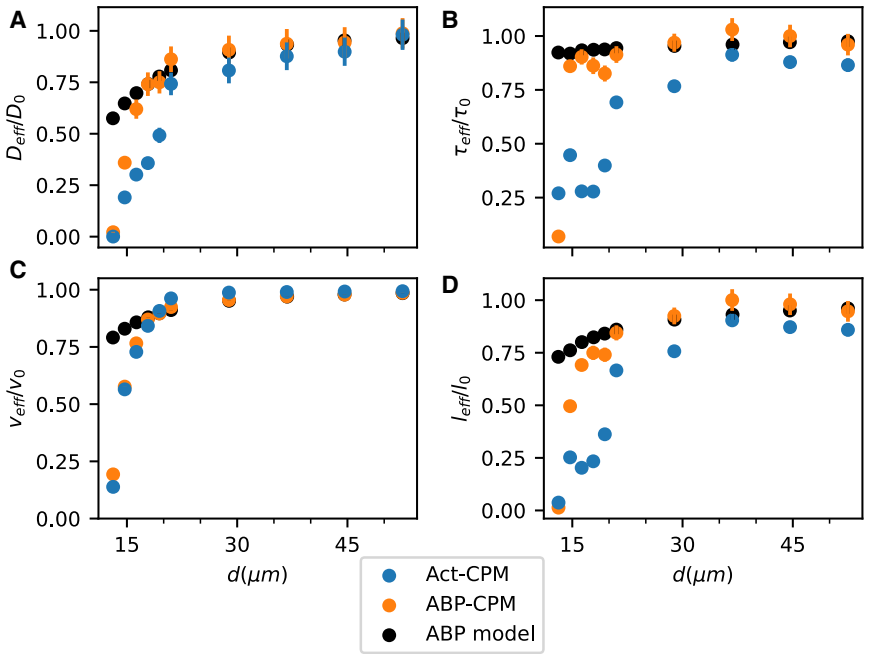

FIGURE 5 Normalized effective parameters of the persistent random walk in regular pillar grids for the Act-CPM, ABP-CPM, and ABP model with the starved parameter settings. (*A*) Effective diffusion coefficient D_{eff} normalized by the diffusion coefficient of starved simulations on an empty field as a function of the distance d between pillar centers. (*B*) Effective persistence time τ_{eff} normalized by the persistence time of starved simulations on an empty field as a function of d. (*C*) Effective instantaneous speed v_{eff} normalized by the instantaneous speed of starved simulations on an empty field as a function of d. (*D*) Effective persistence length $l_{\text{eff}} = v_{\text{eff}}\tau_{\text{eff}}$ normalized by the persistence length of starved simulations on an empty field as a function of d. Error bars indicate 97.5% CI.

Fig. 5 shows the effective motility parameters, or key observables for persistent random motion as a function of pillar distance, of both the CPMs and ABP model, normalized to the motility of each system on a flat substrate. The effective diffusion coefficient D_{eff}, persistence time τ_{eff}, instantaneous speed v_{eff}, and persistence length l_{eff} all increase as a function of increasing pillar distance, and saturate to the corresponding values measured on flat substrates (D_0, τ_0, v_0, and l_0). The speed v_{eff} is a measure of the magnitude of the velocity vector, and thereby motility, where the persistence time τ_{eff} contains information on both the direction and rate of motion; hence, it functions as an indicator for general persistence (35). The effective speed of CPM cells decreases faster than ABPs for small pillar spacings, but does not exhibit a very pronounced difference between the Act-CPM and ABP-CPM. On the contrary, the effective persistence time of the two types of CPM is very dissimilar—the Act-CPM simulations have much shorter persistence times than ABP-CPM tracks at small pillar spacings. Hence, the ABP-CPM system is mainly affected by a decrease in motility, while Act-CPM is affected by both a decrease in persistence and the overall decrease in motility.

Both the deformable cell body and the additional disruption of persistence are key ingredients in enlisting a stronger topotaxtic response than measured for active particles. So far, the CPM models were calibrated to starved *D. discoideum* movement, which typically has a persistence length larger than the cell body. However, when the persistence length of the system is shortened, one expects the contribution of obstacle-induced disruption of persistence to the topotactic drift to decrease, and both types of CPM motility likely result in the same drift. To test this hypothesis, we calibrated the CPM models to represent vegetative *D. discoideum*, which have a much shorter persistence length than their starved counterparts (see appendix A in the supporting material, and Videos S5–S7 for details). Both CPMs predict some topotactic drift (Fig. A3), more than the ABP model, but five times smaller than for the starved simulations. More interestingly, however, there was no clear difference between the two CPM simulations. The cell simulations in regularly spaced grids show that there is indeed a much smaller difference in effective persistence times as a function of pillar spacing, especially for pillar fields spaced apart 16.3 μm or more (Fig. A5). Summarizing, the deformable cell body of CPMs impairs cell speed more during cell-pillar interactions when compared with hard particles, such as ABPs, and enhances topotactic drift. Secondly, methods of motility that are more susceptible to obstacle-induced disruption of persistence lead to even higher topotactic response, as the comparison of Act-CPM and ABP-CPM shows. Finally, setting simulations of vegetative and starved cells side by side shows that, for persistence lengths much shorter than the average cell diameter, any differences in persistence generation hardly contribute to the net topotactic drift, except for the narrowest of pore sizes.

Pillar adhesion influences cell motility and topotactic response

Up to this point, cell-medium and cell-pillar interactions were treated equally in the CPM simulations as the adhesion energies of both components of the cell environment were chosen the same ($J_{\text{cell,pillar}} = J_{\text{cell,medium}}$). However, this

might not properly reflect the response of starved *D. discoideum* to the pillar walls. For one, the live-cell experiments led to a much larger drop in cell speed when going from featureless surfaces to pillar assays compared with the simulations (Fig. 4 *B*). Moreover, previous work (12) has shown that the ameba occasionally explore the vertical pillar walls, which leads to temporary stationary states in persistent cell motion when next to pillars, not unlike the Act-CPM CIL-like interaction between cells and pillars. Drops in speed, lingering behavior next to obstacles, or pillar guidance may be simulated by varying the adhesion energy of pillars relative to the surrounding flat medium $J_{\text{pillar,medium}} \neq J_{\text{cell,medium}}$. During all simulations the cell-medium adhesion energy was kept positive and constant ($J_{\text{cell,medium}} = 20$, see Table 3). Lowering the cell-pillar adhesion energy relative to the cell-medium energy ($J_{\text{pillar,medium}} < J_{\text{cell,medium}}$) promotes occupying lattice sites next to pillars, and thereby encourages cell-pillar adhesion, while discouraging movement into empty medium. Conversely, increasing cell-pillar adhesion energy impedes occupying lattice sites next to pillars, discouraging cell-pillar adhesion and encouraging movement away from pillars into empty medium.

To investigate the effect of modifying the adhesion energy of cell-pillars relative to the surrounding medium, we varied the adhesion parameter $-60 < J_{\text{cell,pillar}} < 50$ around our initial choice $J_{\text{cell,medium}} = J_{\text{cell,pillar}}$ in a topotaxis grid with gradient steepness $s = 0.03$. Examples of simulated cell tracks for more adhesive pillars $J_{\text{cell,pillar}} < 0$ and repelling pillars $J_{\text{cell,pillar}} > J_{\text{cell,medium}}$ are shown in Fig. 6. Clearly, decreasing $J_{\text{cell,pillar}}$ (Fig. 6, *A*, *B*, *D*, and *E*) reduces overall cell displacement in the pillar field, more so for Act-CPM cells than ABP-CPM cells, whereas increasing $J_{\text{cell,pillar}}$ (Fig. 6, *C* and *F*) does not seem to affect cell displacement at first sight (compared with $J_{\text{pillar,medium}} = J_{\text{cell,medium}}$, see Fig. 3, *B* and *E*). The mean coordinates over time (Fig. 6, *G* and *H*) show that the Act-CPM loses its topotactic drift for low $J_{\text{cell,pillar}}$ but not for high $J_{\text{cell,pillar}}$. The ABP-CPM is less affected by high pillar adhesiveness, as it still displays topotactic drift at $J_{\text{cell,pillar}} = -30$.

To further investigate topotaxis for different adhesion energies of pillars, we quantified the topotactic drift v_x and instantaneous velocity $\langle v_{\text{in}} \rangle$ as a function of the difference in adhesive energy between pillars and the medium ($J_{\text{cell,pillar}} - J_{\text{cell,medium}}$). The topotactic drift of Act-CPM cells has a sigmoidal relation to $J_{\text{cell,pillar}} - J_{\text{cell,medium}}$,

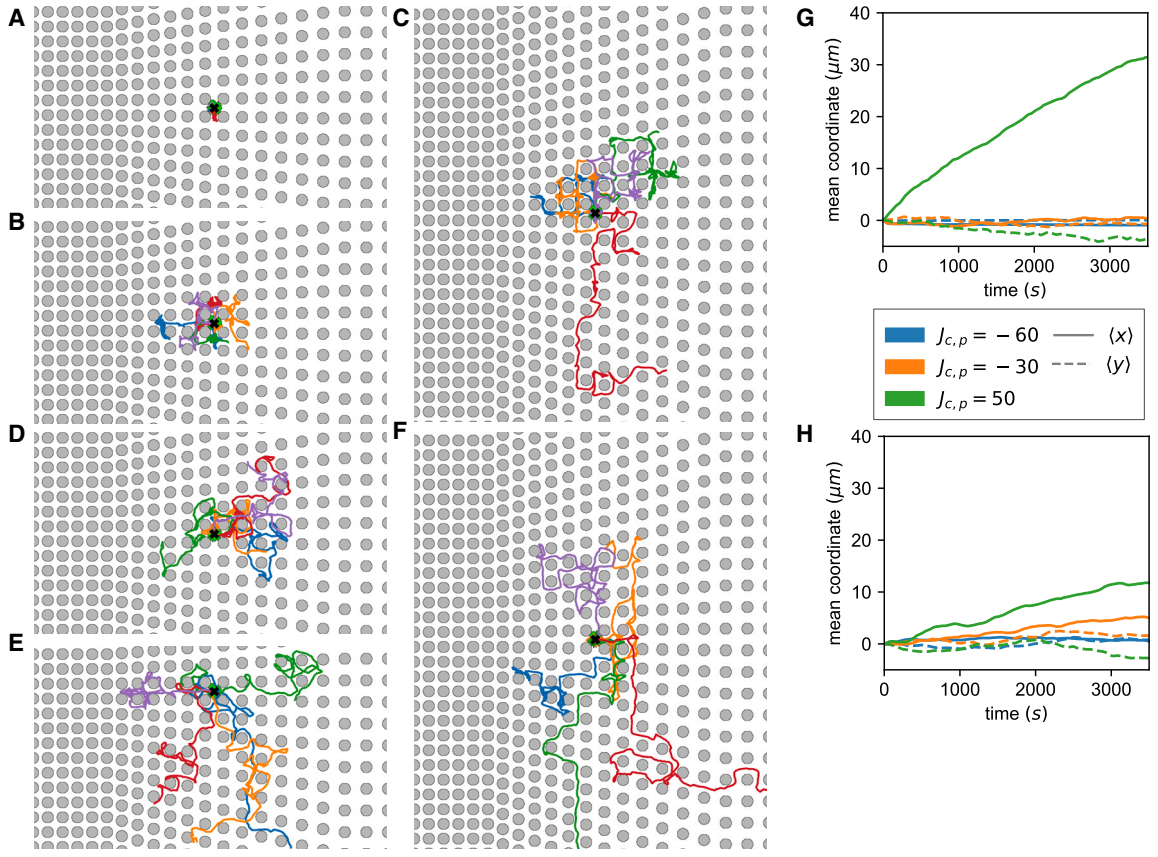

FIGURE 6 Trajectories of starved simulated cells and mean x and y coordinates over time for different pillar adhesion energy $J_{\text{cell,pillar}}$. (*Top row*) Act-CPM example trajectories: (*A*) $J_{\text{cell,pillar}} = -60$, (*B*) $J_{\text{cell,pillar}} = -30$, (*C*) $J_{\text{cell,pillar}} = 50$. (*Bottom row*) ABP-CPM example trajectories: (*D*) $J_{\text{cell,pillar}} = -60$, (*E*) $J_{\text{cell,pillar}} = -30$, (*F*) $J_{\text{cell,pillar}} = 50$. Starting location is marked with a black cross and the depiction of a cell. Each trajectory has its own color. (*Right column*) Mean x and y coordinates over time of 1000 independent simulations for (*G*) Act-CPM and (*H*) ABP-CPM.

whereas the drift v_x of ABP-CPM increases approximately linearly as a function of $J_{\text{cell,pillar}}$. Where the drift of the ABP-CPM population seems to keep increasing as a function of adhesion energy, even beyond its neutral value ($J_{\text{cell,pillar}} - J_{\text{cell,medium}} = 0$), the drift of Act-CPM trajectories quickly plateaus when $J_{\text{cell,pillar}} > J_{\text{cell,medium}}$. Furthermore, high cell-pillar attraction ($J_{\text{cell,pillar}} \ll 0$) has a large effect on the overall motility of Act-CPM cells, as both drift and instantaneous velocity quickly drop to zero for negative adhesion energies (Fig. 7 *B*). Hence, lowering the adhesion energy between cells and pillars can be utilized to model the stationary states in 2D-projected in vitro cell trajectories, and accompanying drop in speed, that occurs when *D. discoideum* explore the vertical pillar walls. The ABP-CPM response in speed is similar to that of Act-CPM, but the cells lose less motility overall at very low cell-pillar adhesion energies; both models seem to share an optimum at $J_{\text{cell,pillar}} = 10$.

The initial aim of varying the cell-pillar adhesion energy was to gauge the effect of the parameter on the strength of topotactic response of the two CPM simulations. In short, decreasing cell-pillar energy negatively affects topotactic drift, and an increase of energy beyond J_{cell} does not affect Act-CPM trajectories, but does enhance the Act-ABP drift. As a final step, we compare the observables of the *D. discoideum* trajectories with the data for the range of adhesion energies investigated (shown in *green* in Fig. 7, *A–C*). The topotactic drift v_x and speed $\langle|v_{ins}|\rangle$ of the models match the experimental data for different adhesion energies, but never at the same energy for both observables (e.g., at $J_{\text{cell,pillar}} = -50$ for v_x and $J_{\text{cell,pillar}} = -70$ for $\langle|v_{ins}|\rangle$ for Act-CPM). The normalized drift $v_x/\langle v_{\text{in}}\rangle$, which scales the topotactic response to the base motility of the system, matches the Act-CPM at $J_{\text{cell,pillar}} - J_{\text{cell,medium}} = -20$, where the ABP-CPM simulations never provide a good fit. Hence, the relative topotactic drift can be approximated using Act-CPM simulations, although it overestimates the base motility of the live-cell data. Overall, the cell-pillar adhesion energy alters cell speed, but lowering speed comes at a cost of decreased topotactic drift, and the adhesion energies at which the experimental values match the observables v_x, $|v_{ins}|$ or $v_x/|v_{ins}|$ are very different between the two CPM simulations.

DISCUSSION

In this study, topotactic drift was measured for starved *D. discoideum* in square lattices of cell-sized pillar obstacles with continuously changing gradients in pillar density. To gain further insight into the underlying physical principles that yield this kind of long-range topotactic drift, the experimental results were followed up by three types of cell simulations in the same anisotropic pillar fields. Topotaxis was simulated using two different CPMs and, to compare with previous work, were accompanied by ABP simulations with the same parameters. The two CPMs modeled persistent random cell motion through two distinct methods of persistence: the Act model with emergent CIL, and an ABP-CPM hybrid, which leaves pillar obstacles without the capacity to alter the inherent persistence of the cells. The motion of simulated cells was matched to the type of persistent random motion of *D. discoideum* by fitting the model parameters to the experimental results on flat PDMS, providing a way to perform order of magnitude comparisons between live-cell and simulated data. The CPM cells had topotactic drifts on a par with the live-cell data, contrary to ABP simulations, which have a much lower topotaxis efficiency. Generally, both the experiments and simulations showed that rising pillar-gradient steepness linearly increases topotactic drift, although there are large differences in the origin and strength of the topotactic response of the three models.

Persistence-driven cellular topotaxis is primarily affected by changes in persistence time

Active Brownian motion on a plane experiencing increasing and decreasing persistence length in opposing directions was previously shown to result in a net drift (16). As undirected cell motility is similar to active Brownian motion at long measurement times (36,37), positionally dependent differences in persistence length are proposed to be a key ingredient of long-range topotaxis (14). In topotaxis simulations by Schakenraad et al., ABPs glide past pillar walls and lose the part of the velocity vector that points in the direction of the pillar center, and thereby some persistence length. Therefore, a gradient in pillar density leads to either larger or smaller losses of velocity depending on gradient position,

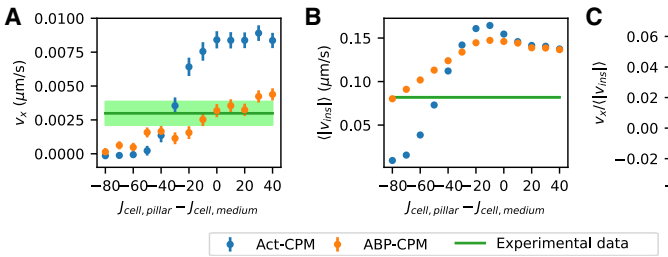

FIGURE 7 Topotactic drift and instantaneous speed of starved parameter set against adhesion preference $J_{\text{cell,pillar}} - J_{\text{cell,medium}}$. For all points $J_{\text{cell,medium}} = 20$. Each data point represents the average of 1000 simulations, error bars indicate 97.5% confidence interval. The line with the shaded area represents the experimental data with 97.5% confidence interval. (*A*) Topotactic drift v_x. (*B*) Instantaneous speed $\langle|v_{ins}|\rangle$. (*C*) Relative topotactic drift $v_x/\langle|v_{ins}|\rangle$.

which, in turn, leads to a net topotactic drift. Cells are not spherical particles, however, and obstacle-induced ABP topotaxis was shown to be accompanied by a much lower normalized drift than measured for highly motile ameba in anisotropic cell-sized pillar fields (12). The difference between both systems is likely caused by the capacity of cell-pillar collisions to influence the intrinsic persistence of the cells, whereas ABPs are merely deflected by pillar walls, always maintaining their inherent constant speed and persistence.

We investigated the influence of including a deformable cell body and changing the method of motility on obstacle-induced changes in the persistence of cell motion. Each of these two factors generally exacerbate changes in persistence length, and thereby topotactic drift, for persistent random cell motion through a pillar gradient, but affect the speed or persistence time differently (Fig. 8). Specifically, comparing the ABP and ABP-CPM shows that the inclusion of a dynamic cell volume alone is not enough to substantially change persistence time as a function of pillar distance. However, including cell volume does cause a drop in effective speed through the more complex pillar interactions such as the cell body embrace of pillars. Moving on to the second factor, when obstacle collisions are allowed to alter incident persistence through using different methods of motility, it does lead to substantial changes in persistence time, as contrasting the Act-CPM and ABP-CPM simulations shows. The Act-CPM CIL cell-pillar interactions lead to a large loss of incident cell polarization, which allows for sharper turns upon collision than the ABP-CPM, which stays more in line with the incident direction of motion. The different methods of motility lead to a large difference in persistence time, although, interestingly, the speed measured during the Act- and ABP-CPM simulations is very similar. The difference in persistence time between the CPMs disappears when the persistence length is decreased beneath the cell diameter (realized by tuning simulations to vegetative *D. discoideum* instead), and the additional contribution of the method of persistence vanishes from the topotactic drift.

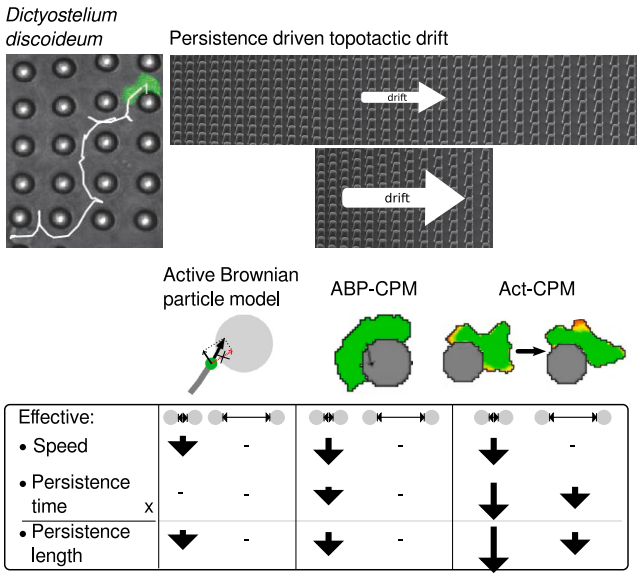

FIGURE 8 Persistence-driven cellular topotaxis results from decrease in effective speed and persistence times in pillar environments. *D. discoideum* shows a drift toward sparser pillar densities in a pillared grid, which we simulated using three models. An ABP model explained this drift as persistence driven, with decreased effective persistence length at short pillar distances due to a drop in effective speed, but does not suffice to describe the magnitude of topotactic drift in experiments. The addition of deformable cell volume in the ABP-CPM results in a larger decrease in effective speed and a decrease in persistence time at short pillar distances, and hence a higher topotactic drift. With its emergent persistent motion, the Act-CPM shows similar changes in effective speed as the ABP-CPM and, moreover, shows a large decrease of effective persistence time at small as well as at larger pillar distances, resulting in the highest topotactic drift.

The reorientation of cells upon obstacle collision has also been the subject of other studies (38–40). In an experiment with fish keratocytes, actin flow was disturbed upon collision with an obstacle, making the keratocyte change direction (38). Modeling studies also indicate that intracellular molecular dynamics are important in cell reorientation upon collision. In Nishimura et al. (39), the change in actin retrograde flow plays an important role in the formation of a new protrusion after collision with a wall, allowing the cell to move away from the wall. In Campbell and Bagchi (40), many different cell behaviors after collision were observed in an immersive boundary method with reaction-diffusion equations on the cell surface. They observed 1) "freezing" when the cell did not have new pseudopods for a short while after collision, 2) "doubling back" when the cell returned in the direction it came from, and 3) "tug of war" when multiple new pseudopods competed for leading the cell's new direction.

Comparing cells on silicon and in silico

Although our primary aim was identifying the key ingredients that uplift ABP topotaxis to cellular topotaxis in cell-sized pillar fields, the method of in-vitro-inspired CPM simulations applied here also has a potential to help discover useful obstacle assays in the future. By first measuring cell motion experimentally on a flat surface, then fitting CPM model parameters to match that motion, and finally predicting the response of cells to an obstacle configuration, the method can serve to predict the response of other cells to different obstacle designs. Using simulations instead of gathering data on in vitro assays, can speed up the design processes of new assays that aim to guide cell motion by obstacles or obstacle adhesiveness to, for example, achieve cell sorting or promote tissue regeneration.

In setting up such simulations, one should strive to minimize any differences between the computational and live-cell results. In this work, we explored if cell-pillar adhesiveness is at the root of the discrepancy in instantaneous speed

between the experiment and the model and if it can be exploited to more accurately model the measured ratio between base motility (speed) and topotactic drift of the experimental data. The instantaneous speed of the simulated cells in both CPMs could be lowered by decreasing the cell-pillar adhesion energy, i.e., by increasing cell-pillar attraction. However, the motility of Act-CPM cells decreases much quicker than in the case of ABP-CPM, where the unaltered base persistence is capable of breaking the cell free from pillar contact. Cell displacement decreases at low adhesion energy leading to a reduced overall topotactic response in both simulations. Conversely, the simulations respond differently to increasing cell-pillar adhesion energy beyond that of the medium, as Act-CPM topotactic drift quickly plateaus to a constant value and ABP-CPM keeps rising at increased energy. It was possible to obtain the same normalized drift as the experimental data by varying the adhesion energy of Act-CPM simulations; however, the concurrence is reached at a slightly different magnitude of the instantaneous velocity and drift.

Despite including a cell body, alterable persistence and pillar adhesion energy delivered the same normalized topotactic drift, our simulations were unable to reproduce the general loss of motility measured for the ameba. The simulations likely do not fully capture the dimensionality and chemotactic intricacies of the in vitro assay. Experimental observation show that *D. discoideum* cells sometimes crawl up a pillar, mainly displacing their center of mass vertically. They can also move through narrower pillar distances than our CPM simulations by spreading their volume vertically. Although vertical displacement is not modeled directly in the 2D CPM, the weight of the area and perimeter constraint can be seen as a measure of 3D flexibility. Yet, 3D versions of the CPM could be used also to compare with experiments on 3D grids. Such grids could either have a confining floor and ceiling, or extended pillars reducing floor and ceiling confinement effects. Next, starved *D. discoideum* secrete and degrade cAMP (41), which acts as a chemoattractant and promotes chemokinesis. Obstacle configurations may nontrivially influence local cAMP concentrations, for example, between pillar domains. Studies have shown that chemotaxis can assist in guiding cell movement around large obstacles (42) or through mazes (43). Furthermore, self-secreted chemoattractants can also trap cells within containing environments such as dead ends in mazes (44). The effect of chemical sensing in a field with a high density of obstacles as well as its effect in topotaxis are still open for study.

Whether topotaxis plays a role during cell migration within multicellular organisms, such as during metastasis or the immune response, remains unclear. There are two major differences with the model system considered here and (metazoan) cells migrating through tissue. The first difference is the influence of the extracellular matrix, which allows cells to actively deform and remodel their surroundings, but also allows for cell adhesion, leading to a more dynamic interaction with obstacles, obstacle density, and adhesion-dependent motility modes (45–47). The second major difference is the relatively large and rigid nucleus of (mammalian) cells in tissue compared with the ameba *D. discoideum* and, as such, was not explicitly taken into account in our models. However, the presence of very small pores does force the cell to not only deform itself but also the nucleus to a large degree, which could (drastically) alter the effective speed and persistence of the cell. Experimental and modeling studies have already provided some insights into the role of nuclear mechanics in squeezing through pores on motility after passage through a pore (48–50), and shown that navigation in 3D obstacle fields is heavily influenced by cell deformability and matrix porosity (40,51), and that matrix deformation and remodeling by migrating cells introduces a nonlinear dependency of persistence time on fiber length and matrix density (52) is necessary for invasion of the lamella (53), and locally stiffens the matrix up multiple cell radii (54). Further experimental and modeling efforts are needed to study how these aspects interact with topotaxis in tissues.

SUPPORTING MATERIAL

Supporting material can be found online at https://doi.org/10.1016/j.bpj.2023.06.001.

AUTHOR CONTRIBUTIONS

L.v.S., J.A.J.W., K.S., D.H., and R.M.H.M. designed the research. L.v.S. performed simulations. J.A.J.W. performed experiments. L.v.S. and J.A.J.W. analyzed the data and wrote the manuscript. D.H. and R.M.H.M. critically revised the manuscript.

ACKNOWLEDGMENTS

We thank SURFsara for the support and computing time in using the Lisa cluster computer. J.A.J.W. and D.H. acknowledge the Fraunhofer Society for the Fraunhofer Attract grant "3DNanoCell" for partly funding this work and thank Dr. Günther Gerisch (Max Planck Institute of Biochemistry, Martinsried, Germany) for providing axenic *D. discoideum (Ax2)* with both free GFP and limGFP in lim0 insertion. R.M.H.M. was funded by the Nederlandse Organisatie voor Wetenschappelijk Onderzoek grant NWO/ENW-VICI 865.17.004.

DECLARATION OF INTERESTS

The authors declare no competing interests.

REFERENCES

1. Pathak, A., and S. Kumar. 2012. Independent regulation of tumor cell migration by matrix stiffness and confinement. *Proc. Natl. Acad. Sci. USA*. 109:10334–10339.
2. Ranamukhaarachchi, S. K., R. N. Modi, …, S. I. Fraley. 2019. Macromolecular crowding tunes 3D collagen architecture and cell morphogenesis. *Biomater. Sci.* 7:618–633.

3. Krummel, M. F., R. S. Friedman, and J. Jacobelli. 2014. Modes and mechanisms of T cell motility: roles for confinement and Myosin-IIA. *Curr. Opin. Cell Biol.* 30:9–16.
4. Toyjanova, J., E. Flores-Cortez, …, C. Franck. 2015. Matrix confinement plays a pivotal role in regulating neutrophil-generated tractions, speed, and integrin utilization. *J. Biol. Chem.* 290:3752–3763.
5. Hellmann, J. K., S. Münter, …, F. Frischknecht. 2011. Environmental constraints guide migration of malaria parasites during transmission. *PLoS Pathog.* 7, e1002080.
6. Battista, A., F. Frischknecht, and U. S. Schwarz. 2014. Geometrical model for malaria parasite migration in structured environments. *Phys. Rev. E.* 90, 042720.
7. Park, J., D. H. Kim, …, A. Levchenko. 2016. Directed migration of cancer cells guided by the graded texture of the underlying matrix. *Nat. Mater.* 15:792–801.
8. Heo, C., C. Jeong, …, T. I. Kim. 2017. Cellular behavior controlled by bio-inspired and geometry-tunable nanohairs. *Nanoscale.* 9:17743–17751.
9. Mahmud, G., C. J. Campbell, …, B. A. Grzybowski. 2009. Directing cell motions on micropatterned ratchets. *Nat. Phys.* 5:606–612.
10. Caballero, D., J. Comelles, …, D. Riveline. 2015. Ratchetaxis: long-range directed cell migration by local cues. *Trends Cell Biol.* 25:815–827.
11. Reversat, A., F. Gaertner, …, M. Sixt. 2020. Cellular locomotion using environmental topography. *Nature.* 582:582–585.
12. Wondergem, J. A. J., M. Mytiliniou, …, D. Heinrich. 2019. Chemotaxis and topotaxis add vectorially for amoeboid cell migration. Preprint at bioRxiv. https://doi.org/10.1101/735779.
13. Li, L., E. C. Cox, and H. Flyvbjerg. 2011. 'Dicty dynamics': Dictyostelium motility as persistent random motion. *Phys. Biol.* 8, 046006.
14. Schakenraad, K., L. Ravazzano, …, L. Giomi. 2020. Topotaxis of active Brownian particles. *Phys. Rev. E.* 101:032602–032611.
15. Berg, H. C., and D. A. Brown. 1972. Chemotaxis in Escherichia coli analysed by three-dimensional tracking. *Nature.* 239:500–504.
16. Novikova, E. A., M. Raab, …, C. Storm. 2017. Persistence-driven durotaxis: generic, directed motility in rigidity gradients. *Phys. Rev. Lett.* 118, 078103.
17. Niculescu, I., J. Textor, and R. J. de Boer. 2015. Crawling and gliding: a computational model for shape-driven cell migration. *PLoS Comput. Biol.* 11, e1004280.
18. Pang, K. M., E. Lee, and D. A. Knecht. 1998. Use of a fusion protein between GFP and an actin-binding domain to visualize transient filamentous-actin structures. *Curr. Biol.* 8:405–408.
19. Palchesko, R. N., L. Zhang, …, A. W. Feinberg. 2012. Development of polydimethylsiloxane substrates with tunable elastic modulus to study cell mechanobiology in muscle and nerve. *PLoS One.* 7, e51499.
20. Bretschneider, T., S. Diez, …, G. Gerisch. 2004. Dynamic actin patterns and Arp2/3 assembly at the substrate-attached surface of motile cells. *Curr. Biol.* 14:1–10.
21. Youssef, S., S. Gude, and J. O. Rädler. 2011. Automated tracking in live-cell time-lapse movies. *Integr. Biol.* 3:1095–1101.
22. Stevense, M., J. R. Chubb, and T. Muramoto. 2011. Nuclear organization and transcriptional dynamics in Dictyostelium. *Dev. Growth Differ.* 53:576–586.
23. Belotti, Y., D. McGloin, and C. J. Weijer. 2021. Effects of spatial confinement on migratory properties of Dictyostelium discoideum cells. *Commun. Integr. Biol.* 14:5–14.
24. Graner, F., and J. A. Glazier. 1992. Simulation of biological cell sorting using a two-dimensional extended Potts model. *Phys. Rev. Lett.* 69:2013–2016.
25. Ouchi, N. B., J. A. Glazier, …, Y. Sawada. 2003. Improving the realism of the cellular Potts model in simulations of biological cells. *Physica A.* 329:451–458.
26. Lee, K. C. 1995. Rejection-free Monte Carlo technique. *J. Phys. A.* 28:4835–4842.
27. Starruß, J., W. de Back, …, A. Deutsch. 2014. Morpheus: A user-friendly modeling environment for multiscale and multicellular systems biology. *Bioinformatics.* 30:1331–1332.
28. Beltman, J. B., A. F. M. Marée, …, R. J. de Boer. 2007. Lymph node topology dictates T cell migration behavior. *J. Exp. Med.* 204:771–780.
29. Zeitz, M., K. Wolff, and H. Stark. 2017. Active Brownian particles moving in a random Lorentz gas. *Eur. Phys. J. E.* 40:23.
30. Maiuri, P., J. F. Rupprecht, …, R. Voituriez. 2015. Actin flows mediate a universal coupling between cell speed and cell persistence. *Cell.* 161:374–386.
31. Takagi, H., M. J. Sato, …, M. Ueda. 2008. Functional analysis of spontaneous cell movement under different physiological conditions. *PLoS One.* 3, e2648.
32. Tweedy, L., B. Meier, …, R. G. Endres. 2013. Distinct cell shapes determine accurate chemotaxis. *Sci. Rep.* 3:2606–2607.
33. Selmeczi, D., S. Mosler, …, H. Flyvbjerg. 2005. Cell motility as persistent random motion: Theories from experiments. *Biophys. J.* 89:912–931.
34. Cherstvy, A. G., O. Nagel, …, R. Metzler. 2018. Non-Gaussianity, population heterogeneity, and transient superdiffusion in the spreading dynamics of amoeboid cells. *Phys. Chem. Chem. Phys.* 20:23034–23054.
35. Stokes, C. L., D. A. Lauffenburger, and S. K. Williams. 1991. Migration of individual microvessel endothelial cells: Stochastic model and parameter measurement. *J. Cell Sci.* 99:419–430.
36. Selmeczi, D., L. Li, …, H. Flyvbjerg. 2008. Cell motility as random motion: A review. *Eur. Phys. J. Spec. Top.* 157:1–15.
37. Campos, D., V. Méndez, and I. Llopis. 2010. Persistent random motion: Uncovering cell migration dynamics. *J. Theor. Biol.* 267:526–534.
38. Vallotton, P., G. Danuser, …, A. B. Verkhovsky. 2005. Tracking retrograde flow in keratocytes: News from the front. *Mol. Biol. Cell.* 16:1223–1231.
39. Nishimura, S. I., M. Ueda, and M. Sasai. 2012. Non-Brownian dynamics and strategy of amoeboid cell locomotion. *Phys. Rev. E.* 85, 041909.
40. Campbell, E. J., and P. Bagchi. 2018. A computational model of amoeboid cell motility in the presence of obstacles. *Soft Matter.* 14:5741–5763.
41. Masaki, N., K. Fujimoto, …, S. Sawai. 2013. Robustness of self-organizing chemoattractant field arising from precise pulse induction of its breakdown enzyme: A single-cell level analysis of PDE expression in Dictyostelium. *Biophys. J.* 104:1191–1202.
42. Grima, R. 2007. Directed cell migration in the presence of obstacles. *Theor. Biol. Med. Model.* 4:2–12.
43. Scherber, C., A. J. Aranyosi, …, D. Irimia. 2012. Epithelial cell guidance by self-generated EGF gradients. *Integr. Biol.* 4:259–269.
44. Marsden, E. J., C. Valeriani, …, D. Marenduzzo. 2014. Chemotactic clusters in confined run-and-tumble bacteria: a numerical investigation. *Soft Matter.* 10:157–165.
45. Wolf, K., M. te Lindert, …, P. Friedl. 2013. Physical limits of cell migration: Control by ECM space and nuclear deformation and tuning by proteolysis and traction force. *J. Cell Biol.* 201:1069–1084.
46. Malandrino, A., X. Trepat, …, M. Mak. 2019. Dynamic filopodial forces induce accumulation, damage, and plastic remodeling of 3D extracellular matrices. *PLoS Comput. Biol.* 15, e1006684.
47. van Steijn, L., I. M. N. Wortel, …, R. M. H. Merks. 2022. Computational modelling of cell motility modes emerging from cell-matrix adhesion dynamics. *PLoS Comput. Biol.* 18, e1009156.
48. Mak, M., C. A. Reinhart-King, and D. Erickson. 2013. Elucidating mechanical transition effects of invading cancer cells with a subnucleus-scaled microfluidic serial dimensional modulation device. *Lab Chip.* 13:340–348.

49. Mak, M., and D. Erickson. 2014. Mechanical decision trees for investigating and modulating single-cell cancer invasion dynamics. *Lab Chip.* 14:964–971.

50. Scianna, M., and L. Preziosi. 2021. A cellular Potts model for analyzing cell migration across constraining pillar arrays. *Axioms.* 10:32.

51. Campbell, E. J., and P. Bagchi. 2021. A computational study of amoeboid motility in 3D: the role of extracellular matrix geometry, cell deformability, and cell–matrix adhesion. *Biomech. Model. Mechanobiol.* 20:167–191.

52. Schlüter, D. K., I. Ramis-Conde, and M. A. J. Chaplain. 2012. Computational modeling of single-cell migration: The leading role of extracellular matrix fibers. *Biophys. J.* 103:1141–1151.

53. Kim, M. C., J. Whisler, …, H. H. Asada. 2015. Cell invasion dynamics into a three dimensional extracellular matrix fibre network. *PLoS Comput. Biol.* 11, e1004535.

54. Tsingos, E., B. H. Bakker, …, R. M. H. Merks. 2023. Hybrid cellular Potts and bead-spring modelling of cells in fibrous extracellular matrix. *Biophys. J.*, in press, accepted: May 10, 2023. https://doi.org/10.1016/j.bpj.2023.05.013.